Available online at www.sciencedirect.com
SCIENCE DIRECT®
Journal of Computational Physics 191 (2003) 622–638
JOURNAL OF COMPUTATIONAL PHYSICS
www.elsevier.com/locate/jcp

SPH simulations of time-dependent Poiseuille flow at low Reynolds numbers

Leonardo Di G. Sigalotti [a,*], Jaime Klapp [b], Eloy Sira [a], Yasmin Meleán [a], Anwar Hasmy [a]

[a] *Centro de Física, Instituto Venezolano de Investigaciones Científicas, IVIC, Km. 11, Carretera Panamericana, Apartado 21827, Caracas 1020A, Venezuela*
[b] *Instituto Nacional de Investigaciones Nucleares, ININ, Km. 36.5, Carretera México-Toluca, Ocoayacac 52045, Estado de México, Mexico*

Received 12 December 2002; received in revised form 28 April 2003; accepted 1 July 2003

Abstract

A *working* Smoothed Particle Hydrodynamics (SPH) formalism for solving the equations of motion of a viscous fluid is presented. The method is based on a standard symmetrized SPH expression for the viscous forces, which involves only first-order derivatives of the kernel through a direct evaluation of the viscous stress tensor. Therefore, the interpolation can be performed using low-order kernels of compact support without compromising the accuracy and stability of the results. In principle, the scheme is suitable for treating compressible fluids with arbitrary shear and bulk viscosities. Here, we demonstrate that when it is combined with the pressure-gradient correction proposed by Morris et al., the method is also suitable for solving the Navier–Stokes equations for incompressible flows without any further assumptions. Simulations using the method show close agreement with the analytic series solutions for plane Poiseuille and Hagen–Poiseuille flows at very low Reynolds numbers. At least for these specific tests, the results obtained are essentially independent of employing either a cubic or a quintic spline kernel.

Keywords: Conservation laws; Navier–Stokes equations; Compressible and incompressible viscous fluids; Numerical methods; Stability and convergence of numerical methods

1. Introduction

Laminar flows through channels and pipes are of great practical interest because they often appear in a wide range of industrial, environmental, and biological processes. Many applications to the fields of mechanical, chemical, and petroleum engineering involve slow viscous incompressible flows through ducts,

* Corresponding author. Tel.: +58-0212-5041369; fax: +58-0212-5041148.
E-mail addresses: lsigalot@cassini.ivic.ve (L.D.G. Sigalotti), klapp@nuclear.inin.mx (J. Klapp), esira@hubble.ivic.ve (E. Sira), meleany@manare.ivic.ve (Y. Meleán), anwar@ivic.ve (A. Hasmy).

0021-9991/$ - see front matter © 2003 Elsevier B.V. All rights reserved.
doi:10.1016/S0021-9991(03)00343-7

filters, substrates, porous materials, and other devices. Therefore solutions to the Navier–Stokes equations describing the behavior of such flows are of fundamental importance.

A number of exact solutions to these equations can be found in the classical literature [1,2]. Among these solutions, a special case is represented by three-dimensional (3D) Hagen–Poiseuille flow in a capillary tube of circular cross-section. In these flows, the volumetric flow rate is proportional to the pressure change along the tube. In fact, it was the research on blood flow in animal capillaries that first revealed this relationship. In mammals, blood flow in veins and air flow in lung alveoli are some examples of Hagen–Poiseuille flow. Other practical examples can be found, as for instance, the flow through a soda straw or through a hypodermic needle. The two-dimensional (2D) analogue of laminar flow in circular tubes is provided by the well-known plane Poiseuille flow, i.e., viscous fluid flow between fixed parallel walls. In particular, this solution has applications to flow through channel systems.

In this paper, we are primarily concerned with numerical calculations of time-dependent, plane Poiseuille flow and Hagen–Poiseuille flow at very low Reynolds number ($Re \ll 1$) using the method of Smoothed Particle Hydrodynamics (SPH). While this method has originally been devised to simulate compressible fluids for astrophysical applications [3,4], it has recently been applied to a large variety of problems in continuum mechanics [5–11]. However, most earlier applications of the method were limited to inviscid flows due to its apparent inability to treat viscosity in a rigorous manner. The reason was in the difficulty of finding stable and accurate SPH representations for the second-order spatial derivatives of the velocity appearing in the viscous forces. A disadvantage of using straightforward second derivatives of the kernel is that the interpolation becomes susceptible to transverse mode instabilities at low resolution especially when low-order kernels of compact support are employed [12]. Since the stability properties of SPH depend on the second derivatives of the kernel, the growth of the unstable modes is highly reduced for smoother kernels, and eventually disappear when a Gaussian kernel is used to perform the interpolation. In particular, Takeda et al. [7] proposed an SPH formalism for solving the Navier–Stokes equations for constant viscosity based on direct evaluation of the second derivatives of *a Gaussian kernel*. However, it is well known that most SPH simulations employ low-order kernels, such as the cubic spline kernel originally proposed by Monaghan and Lattanzio [13]. Therefore, it would be desirable to implement working formulations for kernels of compact support. Attempts in this direction have been made by Flebbe et al. [14] and Watkins et al. [15], who devised independent methods for treating a general viscosity based on standard SPH expressions for first derivatives. In their schemes, it is not only possible to specify the shear and bulk viscosity as separate arbitrary parameters, but also to employ a cubic spline kernel without the occurrence of significant instability.

Although the above methods have successfully been applied to model compressible gases with $Re \approx 5$ [7,15], it was not clear that SPH could be extended to the simulation of incompressible fluids with $Re \ll 1$. A first attempt to model such flows was reported by Morris et al. [9], who derived a modified SPH formalism relying on an appropriate pressure-gradient correction along with a diffusion-like SPH estimation of the viscous forces in which direct evaluation of second-order derivatives is not required. Recently, we have tried and tested an SPH formalism which works equally well for both compressible and incompressible viscous flows. The formulation is based on standard symmetrized SPH expressions for the viscous forces and viscous energy generation which are variationally consistent with the usual kernel smoothing for the density [16]. This is one basic difference compared to the method of Flebbe et al. [14], which uses an antisymmetric SPH representation to evaluate the viscous forces. They claim that such a representation yields improved linear and angular momentum conservation. However, in their scheme the coupling of the resulting SPH equations of motion with the second-order kernel smoothing for the density results in a formalism which is not variationally consistent according to the analysis of Bonet and Lok [16]. In particular, these latter authors have shown that the variation of the total potential energy of the system provides a framework for the derivation of the internal forces. Since this can be expressed in terms of the variation of the density, the resulting SPH representation for the internal

forces is seen to depend on whether the density is evaluated by means of its smoothing kernel summation or by solving the continuity equation. It is important to note that not all the SPH expressions found in the literature can actually be derived from a potential. The use of a variationally consistent SPH scheme addresses the momentum preservation properties in the absence of external forces provided that the total energy functional is invariant with respect to solid body motions. Whereas translational invariance is usually satisfied by most existing SPH schemes, appropriate corrections to the kernel and its gradients, not yet implemented in our code, would be necessary to guarantee invariance of the internal energy function and hence improved conservation of the angular momentum [16]. The use of symmetrized representations for the equations of motion and energy coupled with a smoothed representation for the density will always result in a variationally consistent SPH scheme in which momentum preservation can be addressed properly. If, on the contrary, antisymmetric representations like those implemented by Flebbe et al. [14] are used, variational consistency would demand solving the continuity equation rather than using a kernel smoothing for the density. Unlike the method of Watkins et al. [15], the present scheme involves direct evaluation of the viscous stress tensor which in turn may be expanded in SPH form using standard expressions for first derivatives. When this scheme is combined with the pressure-gradient correction advanced by Morris et al. [9], it can also be applied to model incompressible flows. The scheme reproduces the analytic series solution for unsteady plane Poiseuille and Hagen–Poiseuille flows at very low ($Re \ll 1$) and moderate ($Re > 1$) Reynolds numbers. The results show that even a cubic spline kernel can be used without the occurrence of significant noise in the pressure and velocity fields. The method is also shown to perform well when applied to the formation of a liquid drop for a van der Waals fluid in two dimensions.

2. SPH formulation

In this section, we shall briefly describe a working SPH formulation for solving the equations of motion of a viscous fluid. In particular, the method can be used for simulating compressible ($Re > 1$) and incompressible ($Re < 1$) flows alike.

In general, SPH is a gridless Lagrangian method based on interpolation theory. The conservation laws of continuum dynamics, in the form of partial differential equations, are transformed into integral equations through the use of an interpolation function that gives the kernel estimate of the field variables at a point. Computationally, the integrals are evaluated as sums over neighboring particles. For instance, the continuous density field at the location of particle "a", say $\rho_a = \rho(\mathbf{r}_a)$, is estimated according to

$$\rho_a = \sum_{b=1}^{N} m_b W_{ab}, \tag{1}$$

where the summation is over N neighboring particles around particle "a" (including it), m_b is the mass of particle "b", and $W_{ab} = W(|\mathbf{r}_{ab}|, h)$ is the kernel interpolation function. Here, $\mathbf{r}_{ab} = \mathbf{r}_a - \mathbf{r}_b$ is the distance between particles a and b, and h is the so-called smoothing length which specifies the width $2h$ of the kernel. Within second-order accuracy, Eq. (1) replaces the continuity equation. If Eq. (1) is chosen to evaluate the density, variational consistency demands using a symmetrized SPH representation for the equations of motion [16].

The general equations governing the motion of a viscous fluid element can be written using the standard index-summation convention as:

$$\frac{\mathrm{d}v^i}{\mathrm{d}t} = \frac{1}{\rho}\frac{\partial T^{ij}}{\partial x^j} + F^i, \tag{2}$$

where v^i denotes the ith component of the velocity, T^{ij} is the stress tensor, F^i is the ith component of a body force per unit mass, and x^j is the jth Cartesian component of the position vector $\mathbf{r}$. The stress tensor is written as

$$T^{ij} = -p\delta^{ij} + \sigma^{ij}, \tag{3}$$

where p is the internal pressure, δ^{ij} is the unit tensor, and σ^{ij} is the viscous stress tensor given by

$$\sigma^{ij} = \eta\left(\frac{\partial v^i}{\partial x^j} + \frac{\partial v^j}{\partial x^i}\right) + \left(\zeta - \frac{2}{3}\eta\right)(\nabla\cdot\mathbf{v})\delta^{ij}, \tag{4}$$

with η and ζ being the coefficients of shear and bulk viscosity, respectively. In vector notation form Eq. (2) can be written as

$$\frac{\mathrm{d}\mathbf{v}}{\mathrm{d}t} = \frac{1}{\rho}\nabla\cdot\mathbf{T} + \mathbf{F}. \tag{5}$$

A standard symmetrized SPH representation of this equation can be derived using the identity

$$\frac{1}{\rho}\nabla\cdot\mathbf{T} = \nabla\cdot\left(\frac{\mathbf{T}}{\rho}\right) + \left(\frac{\mathbf{T}}{\rho^2}\right)\cdot\nabla\rho.$$

Replacing this form into the right-hand side of Eq. (5) and using the standard SPH expressions

$$\left[\nabla\cdot\left(\frac{\mathbf{T}}{\rho}\right)\right]_a = \sum_{b=1}^{N} m_b\frac{\mathbf{T}_b}{\rho_b^2}\cdot\nabla_a W_{ab}, \tag{6}$$

$$\left[\frac{\mathbf{T}}{\rho^2}\cdot\nabla\rho\right]_a = \frac{\mathbf{T}_a}{\rho_a^2}\cdot\sum_{b=1}^{N} m_b\nabla_a W_{ab}, \tag{7}$$

we obtain the following SPH representation for the equations of motion

$$\frac{\mathrm{d}\mathbf{v}_a}{\mathrm{d}t} = \sum_{b=1}^{N} m_b\left(\frac{\mathbf{T}_a}{\rho_a^2} + \frac{\mathbf{T}_b}{\rho_b^2}\right)\cdot\nabla_a W_{ab} + \mathbf{F}_a, \tag{8}$$

where $\mathbf{v}_a = \mathbf{v}(\mathbf{r}_a)$ is the velocity of particle a and ∇_a is the gradient operator at its location. This symmetrized form has been demonstrated to be variationally consistent with the use of Eq. (1) for the density [16]. The expression on the right-hand side of Eq. (8) can be easily implemented since it requires only a direct evaluation of the viscous stress tensor (4), which in turn can be expanded in complete SPH form using the standard expressions

$$(\nabla\mathbf{v})_a = \frac{1}{\rho_a}\sum_{b=1}^{N} m_b(\mathbf{v}_b - \mathbf{v}_a)\nabla_a W_{ab} \tag{9}$$

and

$$(\nabla\cdot\mathbf{v})_a = \frac{1}{\rho_a}\sum_{b=1}^{N} m_b(\mathbf{v}_b - \mathbf{v}_a)\cdot\nabla_a W_{ab} \tag{10}$$

for the velocity gradient and divergence, respectively. In passing we note that, like the schemes proposed by Flebbe et al. [14] and Watkins et al. [15], the SPH Eq. (8) can be used independently on whether the shear

and bulk viscosity coefficients are constant, as in the Navier–Stokes equations, or arbitrary varying functions of the coordinates. Furthermore, since direct evaluation of second-order derivatives of the kernel is not required, the method permits the use of low-order interpolating kernels of compact support without compromising the stability and the accuracy of the calculation even in the case of very small Reynolds numbers.

For negligible heat exchange between different parts of the fluid, Eqs. (1) and (8) are enough to completely describe the flow for given boundary conditions once an equation of state relating the density and the pressure is specified. In general, incompressible fluids have a speed of sound c much greater than the speed v of bulk flow, implying that relative fluctuations in density $\delta\rho/\rho$, which are proportional to the square of the Mach number $M = v/c$, are very small [2]. In fact, this is the case for fluids like water for which $c \sim 10^3$ m s^{-1}. In SPH, where the pressure is obtained using an explicit function of density, local variations in the pressure gradient may force particle motions due to local density gradients. Therefore, it is customary to approximate the flow by an artificial fluid which is exactly incompressible. This is done by introducing a dynamic pressure p [9], such that $p = p_{\mathrm{T}} - p_{\mathrm{H}}$, where p_{T} is the total pressure and p_{H} refers to the hydrostatic pressure. Since the pressure enters as a gradient in the equations of motion, we have that

$$-\frac{1}{\rho}\nabla p_{\mathrm{T}} = -\frac{1}{\rho}\nabla p - \frac{1}{\rho}\nabla p_{\mathrm{H}} = -\frac{1}{\rho}\nabla p + \mathbf{F}, \tag{11}$$

where the effect of p_{H} is that of a body force and the dynamic pressure is modeled using the simple equation of state

$$p = c^2\rho. \tag{12}$$

The sound speed c is chosen such that it is sufficiently large to ensure that the behavior of the corresponding incompressible fluid is close enough to that of the real fluid, yet not so large to avoid prohibitively small timesteps. From the balance of forces in the Navier–Stokes equations, it can be readily shown that c^2 in Eq. (12) is given by the largest of the three quantities:

$$\frac{v_0^2}{\delta}, \quad \frac{vv_0}{L_0\delta}, \quad \frac{L_0|\mathbf{F}|}{\delta}, \tag{13}$$

where L_0 is some typical length scale of the flow, v_0 is a typical velocity, $\delta = \delta\rho/\rho_0$, and $\mathbf{F}$ is a body force per unit mass. With this choice of the sound speed, density fluctuations are effectively limited to within $\sim$3% for most practical applications. Furthermore, since $p \ll p_{\mathrm{H}}$, Eq. (11) amounts to a small correction to keep numerical fluctuations in the density below a certain level. It is precisely this correction, first proposed by Morris et al. [9], which allows us to use the SPH representation (8) for very low *Re* flows without any further assumptions.

In flows where the effects of heat conduction are important Eq. (2) must be complemented with a further differential equation for the time rate of change of the internal energy, namely

$$\frac{\mathrm{d}U}{\mathrm{d}t} = \frac{1}{\rho}T^{ij}\frac{\partial v^i}{\partial x^j} - \frac{1}{\rho}\frac{\partial q^k}{\partial x^k}, \tag{14}$$

where U is the specific internal energy and q^k is the kth component of the heat flux vector $\mathbf{q} = -\kappa\nabla\mathcal{T}$, where κ is the coefficient of thermal conductivity and $\mathcal{T}$ is the fluid temperature. All other variables in Eq. (14) have the same meaning as before. In vector form, Eq. (14) can be written as

$$\frac{\mathrm{d}U}{\mathrm{d}t} = \frac{1}{\rho}\mathbf{T} : \nabla\mathbf{v} - \frac{1}{\rho}\nabla\cdot\mathbf{q}, \tag{15}$$

where the colon indicates a double dot product. In order to keep the variational consistency of the scheme, a symmetrized SPH representation of Eq. (15) must also be implemented. This is readily done by means of the two identities:

$$\frac{1}{\rho}\nabla\cdot\mathbf{q}=\nabla\cdot\left(\frac{\mathbf{q}}{\rho}\right)+\frac{\mathbf{q}}{\rho^2}\cdot\nabla\rho,$$

and

$$\frac{\mathbf{T}}{\rho}:\nabla\mathbf{v}=\nabla\cdot\left(\frac{\mathbf{T}}{\rho}\cdot\mathbf{v}\right)-\mathbf{v}\cdot\left(\nabla\cdot\frac{\mathbf{T}}{\rho}\right).$$

The terms on the right-hand side of the first identity admit the same SPH forms given by Eqs. (6) and (7) with the tensor $\mathbf{T}$ replaced by the vector $\mathbf{q}$. The term on the left-hand side of the second identity can be put in SPH form as

$$\left(\frac{1}{\rho}\mathbf{T}:\nabla\mathbf{v}\right)_a=\sum_{b=1}^{N}m_b\frac{\mathbf{T}_a}{\rho_a^2}:(\mathbf{v}_b-\mathbf{v}_a)\nabla_a W_{ab}, \tag{16}$$

while those on the right-hand side take the form

$$\left[\nabla\cdot\left(\frac{\mathbf{T}}{\rho}\cdot\mathbf{v}\right)\right]_a-\left[\mathbf{v}\cdot\left(\nabla\cdot\frac{\mathbf{T}}{\rho}\right)\right]_a=\sum_{b=1}^{N}m_b\frac{\mathbf{T}_b}{\rho_b^2}:(\mathbf{v}_b-\mathbf{v}_a)\nabla_a W_{ab}, \tag{17}$$

where we have used the further identity $\mathbf{T}\cdot\mathbf{v}\cdot\nabla W=\mathbf{T}:\mathbf{v}\nabla W$. On averaging the right-hand sides of Eqs. (16) and (17), we finally obtain the symmetrized SPH representation of the specific internal energy equation

$$\frac{\mathrm{d}U_a}{\mathrm{d}t}=\frac{1}{2}\sum_{b=1}^{N}m_b\left(\frac{\mathbf{T}_a}{\rho_a^2}+\frac{\mathbf{T}_b}{\rho_b^2}\right):(\mathbf{v}_b-\mathbf{v}_a)\nabla_a W_{ab}-\sum_{b=1}^{N}m_b\left(\frac{\mathbf{q}_a}{\rho_a^2}+\frac{\mathbf{q}_b}{\rho_b^2}\right)\cdot\nabla_a W_{ab}, \tag{18}$$

where $U_a=U(\mathbf{r}_a)$ is the specific internal energy of particle a. The heat flux vector $\mathbf{q}$ is expanded in SPH form using a representation for the temperature gradient identical to that of Eq. (9) for the velocity.

An SPH formulation based on expressions similar to Eqs. (8) and (18) have been implemented by Libersky et al. [17] to simulate the response of elastic–plastic solids to induced large deformations. A 2D version of this formulation using cylindrical coordinates has also been presented by Petschek and Libersky [18]. In the former approach, the SPH representation of the force equation is identical in form to Eq. (8), while for the specific internal energy they use an antisymmetric SPH representation based on an expansion like that given by Eq. (17) for the viscous energy generation term. In their scheme, however, the density is obtained by solving the continuity equation. Since their formulation is applicable to the dynamics of deformable elastic bodies, the constitutive relations in their code are much more complicated than the ones needed here for simulation of a viscous fluid. In particular, an extra differential equation for the time rate of change of the deviatoric stress must be added in order to follow the material response to deformations due to strain and rotations. This equation along with appropriate constitutive equations for the pressure p and elastic potential energy U will then be necessary to generalize the present scheme for simulating large distortions of an elastic medium and debris cloud from hypervelocity impacts on solids.

3. Time-dependent Poiseuille flow

A very sensitive test to check the reliability and accuracy of the method illustrated above is provided by Poiseuille flow between parallel plates and in a circular pipe at low Reynolds numbers. These test cases have been chosen because they allow for a direct comparison with analytically constructed solutions for unsteady flows. Numerical SPH calculations of plane Poiseuille and Hagen–Poiseuille flows have been performed by Takeda et al. [7], Morris et al. [9], and Watkins et al. [15].

3.1. Plane Poiseuille flow

We first consider unsteady flow between two infinite, parallel plates at rest in presence of a pressure gradient. We choose the (x,y)-plane to represent the flow and the positive x-axis as the flow direction, with the plates being located at distances $y=\pm d$ from the center ($y=0$) of the coordinate system. For this specific problem, both the velocity component v_y and the pressure gradient in the vertical y-direction vanish identically so that the x-component of the velocity depends only on y and time t. In this simple case, the Navier–Stokes equations admit the exact time-dependent solution

$$v_x(y,t)=\frac{|\mathbf{F}|}{2\nu}\left(y^2-d^2\right)+\sum_{n=0}^{\infty}\frac{16(-1)^n d^2|\mathbf{F}|}{\nu\pi^3(2n+1)^3}\cos\left[\frac{(2n+1)\pi y}{2d}\right]\exp\left[-\frac{(2n+1)^2\pi^2\nu t}{4d^2}\right], \tag{19}$$

where d is half the separation of the plates, $\nu=\eta/\rho$ is the coefficient of kinematic viscosity, and $\mathbf{F}$ is a force per unit mass given by

$$|\mathbf{F}|=\frac{1}{\rho}\frac{\partial p}{\partial x}=\frac{1}{\rho}\left(\frac{\Delta p}{L}\right)=-\frac{2\nu v_0}{d^2}, \tag{20}$$

where Δp is the pressure difference in the x-direction between two points separated by a length L and v_0 is a constant asymptotic velocity defined by

$$v_0=-\frac{d^2}{2\rho\nu}\left(\frac{\Delta p}{L}\right). \tag{21}$$

Note that $\Delta p<0$ and hence v_0 is a positive quantity. Since the flow is incompressible the density remains uniform ($\rho=\rho_0$) and the sound speed takes the form

$$c^2=c_0^2-\frac{2\nu v_0}{d^2}x=c_0^2+|\mathbf{F}|x. \tag{22}$$

Comparing Eq. (22) with Eqs. (11) and (12), we see that the flow is effectively driven by an applied body force which is here identified with the hydrostatic pressure gradient $\Delta p/L=-2\nu\rho_0 v_0/d^2$.

For large times ($t\to\infty$), the series expansion in Eq. (19) vanishes and the velocity approaches the well-known steady-state solution

$$v_x(y)=\frac{|\mathbf{F}|}{2\nu}\left(y^2-d^2\right)=v_0\left(1-\frac{y^2}{d^2}\right), \tag{23}$$

with v_0 as given by Eq. (21). We see that the velocity tends to an asymptotic parabolic profile, with the vertex of the parabola (at $y=0$) moving in the direction of the flow with velocity v_0. At $y=\pm d$, $v_x=0$ and the liquid sticks to the walls. Thus, if at time $t=0$, the particles are on a plane cross-section, i.e., initially with zero velocity, they will flow into a sequence of parabolic profiles until the asymptotic, steady-state solution (23) is achieved.

The method in Section 2 was used to follow this transient behavior. In particular, we study the case of very low Reynolds number and perform several tests with initial parameters similar to those employed by Morris et al. [9]. With the choice of $Re = 0.0125$, $2d = 1.0 \times 10^{-3}$ m, $\rho_0 = 1.0 \times 10^3$ kg m^{-3}, and $v_0 = 1.25 \times 10^{-5}$ m s^{-1}, the kinematic viscosity is $v = 2dv_0/Re = 1.0 \times 10^{-6}$ m^2 s^{-1}. Setting $c_0 = \alpha v_0$ with $\alpha = 2$, gives a subsonic flow with Mach number $M = 0.5$ such that the pressure along the flow direction becomes

$$p(x) = v_0\rho_0\left(\alpha v_0 - \frac{2v}{d^2}x\right). \tag{24}$$

Eqs. (22)–(24) are the same as Eqs. (3.1) of Takeda et al. [7]. We performed calculations for two different kernel interpolation functions: the cubic spline kernel proposed by Monaghan and Lattanzio [13] and the higher-order quintic spline kernel employed by Morris et al. [9]. Since the stability properties of SPH depend strongly upon the second derivatives of the kernel, we expect improved results for the higher-order quintic spline. In both cases, the calculations were made using 915 particles spanning the channel from $x = 0$ to $x = L$, with $L = 2.33 \times 10^{-4}$ m. For simplicity, we assume that the particles are initially at rest and arranged in a regular Cartesian mesh, with 61 particles along the separation distance between the plates and 15 particles along the length L, yielding an interparticle separation of $\approx 1.7 \times 10^{-5}$ m in both directions. The particles were given a smoothing length h ($\approx 1.73 \times 10^{-5}$ m) chosen to give each particle 12 neighbors all within a circle of radius $2h$. For particles near the surface of the rigid walls ($y = \pm d$), deficiencies in the kernel estimate of the density through the use of Eq. (1) were addressed by placing a collection of imaginary particles just outside the calculation region ($y > |d|$). Accurate results for the kernel estimate of the density for particles near the rigid walls were obtained by defining four consecutive rows of 15 imaginary particles each along the length L on both sides just outside the channel and with the same initial separation as used for the interior particles. Each row of imaginary particles is extended into the regions $x < 0$ and $x > L$ by adding four more particles on each side, giving a total number of 23 imaginary particles per row. Each imaginary particle is given a density ρ_0 equal to the value of its closest image inside the channel. The x-velocity component v_i of the imaginary particle i is calculated from the value of its closest image within the channel, say v_a, by means of the interpolation $v_i = -d'v_a/d$, where d' and d are, respectively, the distances from the wall surface to particles i and a. That way, a linear variation with y is allowed to the velocity of each imaginary particle such that the velocity vanishes exactly at $y = \pm d$. This method is the same as that used by Takeda et al. [7]. Inlet and outlet boundary conditions during the calculation were handled by means of a cyclic boundary condition which is enforced by placing four columns of 61 imaginary particles each along the y-direction to the left ($x < 0$) and to the right($x > L$) of the calculation region. After each timestep, the information carried by the interior particles in the two columns that are closest to the exit of the pipe is automatically mapped into the two columns of imaginary particles that are closest to the pipe entrance. Thus, for each particle exiting the pipe there is another entering on the other side which carries its information. In order to preserve the total number of particles, as the exiting particle leaves the pipe and enters into the outlet set of imaginary particles, there will be one particle of this set which is removed and placed into the inlet set to compensate that which enters the pipe. In practice, this is equivalent to being following the flow through a pipe of infinite length.

In Fig. 1, we show the results of the transient behavior for a sequence of times until 1.0 s, when the velocity profile reaches its steady-state regime given by Eq. (23). The numerical solution (filled dots) is compared with the exact one (solid curves) as calculated from Eq. (19). The dots on each curve are obtained by averaging over neighboring particles. This is done by taking a section of channel of size $\Delta x = L/20$ at about half its total length. The resulting volume is subdivided into 21 rectangular cells, each of width $\Delta y = 2d/21$, distributed along the separation between the walls. With this resolution, the dots at the center of each cell are obtained by averaging over about three particles. Compared with the exact solution, the maximum relative error in the velocity is about 0.7% during the transient and improves to 0.1% for the

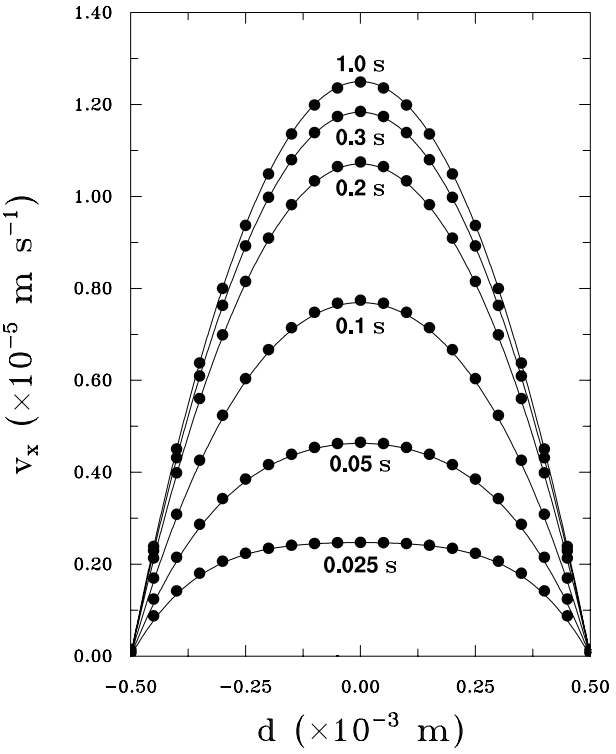

Fig. 1. Numerically obtained velocity profiles (filled dots) compared to the analytical solution (solid curves) for 2D plane Poiseuille flow with $Re = 0.0125$. A sequence of times is shown for the transient evolution. The steady-state solution is reached at about 1 s.

steady-state solution at 1.0 s. In particular, the asymptotic value v_0 (at 1.0 s) is obtained with a relative error of $\sim 8.4 \times 10^{-3}\%$. For the same test, Morris et al. [9] obtained a maximum relative error of 0.7% for the steady-state solution which is about seven times larger than that obtained here. Furthermore, the maximum and minimum calculated densities are $\rho_{\max} = 1.004\rho_0$ and $\rho_{\min} = 0.999\rho_0$, respectively, so that the incompressibility of the flow is very well reproduced by the numerical scheme. We also note that the points of contact with the solid walls remain fixed in space and time, a feature of the solution which is also accurately reproduced by the calculations. The results displayed in Fig. 1 were obtained using the cubic spline kernel. Almost identical results were obtained using the quintic spline kernel, meaning that at least for this test case, a piecewise-linear approximation to the second derivatives of the kernel seems to be adequate.

The ability of the scheme to simulate compressible flows was first tested by repeating the previous calculation at a much higher Reynolds number. For this test, we choose $Re = 5$ in order to compare with the results of Watkins et al. [15]. This value is 400 times higher than the one used above. Such a high value is obtained by decreasing the kinematic viscosity to $\nu = 2.5 \times 10^{-9}$ m^2 s^{-1}, while keeping all other initial parameters the same. The calculation was carried out using a cubic spline kernel with the same number of particles and treatment of boundary conditions as described above. The transient behavior for this test model is shown in Fig. 2, where the numerically calculated velocity profile is compared with the analytical solution at different times until 230 s when the steady-state solution is achieved. We note that by increasing the value of Re, the timescale of the transient also increases. For the first five times shown in Fig. 2, the velocity at the vertex of the parabolae is accurately reproduced within a relative error less than $3.3 \times 10^{-2}\%$. At 80 s, the maximum and minimum calculated densities are $\rho_{\max} = 1.025\rho_0$ and $\rho_{\min} = 0.974\rho_0$, respec-

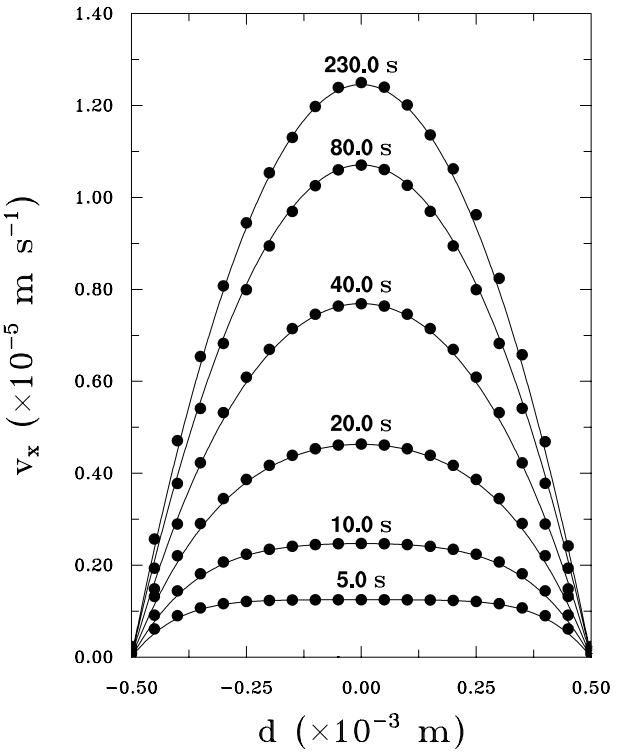

Fig. 2. Numerically obtained velocity profiles (filled dots) compared to the analytical solution (solid curves) for 2D plane Poiseuille flow with $Re = 5$. A sequence of times is shown for the transient evolution. The steady-state solution is reached at about 230 s.

tively. As the calculation is continued, the range of the density variations increases to $0.920\rho_0 \leqslant \rho \leqslant 1.089\rho_0$ by 230 s when the flow approaches its asymptotic stationary profile. At this time, the analytical value of $v_0 (= 1.25 \times 10^{-5}\ \mathrm{m\,s^{-1}})$ is obtained within a relative error of about 0.35%. This large error is due to oscillations of the velocity about the steady-state solution. These oscillations are in turn due to local expansions and contractions of the flow which make the particles to develop velocities that are alternately above and below the corresponding stationary value. This behavior is seen to continue after 230 s, with the oscillations becoming progressively more rapid until the solution eventually becomes unstable by about 280 s. The results for this test are qualitatively similar to those reported by Watkins et al. [15] for plane Poiseuille flow at $Re \sim 5$. Although a detailed comparison with their test is not possible because of the lack of quantitative information in the description of their results, we see that the salient features of the evolution are qualitatively reproduced here and that the stationary parabolic profile in their Fig. 4 compares reasonably well with the one shown in Fig. 2 at 230 s.

3.2. Hagen–Poiseuille flow

As a further test, we consider unsteady laminar flow in a circular pipe of radius R. We choose cylindrical coordinates (r, ϕ, z) to represent the flow and the positive z-axis as the flow direction. With this geometry, the flow is homogeneous along both the z and ϕ coordinates, and so the velocity components v_r, v_ϕ as well as the radial and azimuthal pressure gradients vanish identically. In this way, the z-component of the velocity depends only on radius r and time t. For this case, the Navier–Stokes equations admit the following exact time-dependent solution

$$v_z(r,t) = \frac{|\mathbf{F}|}{4\nu}(r^2 - R^2) + \sum_{m=1}^{\infty} \frac{|\mathbf{F}|R^2}{\nu\alpha_m^2} \frac{J_2(\alpha_m)}{J_1^2(\alpha_m)} J_0\left(\frac{r\alpha_m}{R}\right) \exp\left[-\frac{\nu\alpha_m^2 t}{R^2}\right], \tag{25}$$

where the J_n (with $n = 0, 1, 2$) are Bessel functions of the first kind of integral order n and the $\alpha_m = Rk_m$ (for $m = 1, 2, \ldots$) are the roots of $J_0(kr)$. The other quantities have the same meaning as in Eq. (19). The body force $\mathbf{F}$ now obeys the relation

$$|\mathbf{F}| = -\frac{4\nu v_0}{R^2}, \tag{26}$$

where v_0 is a constant asymptotic velocity given by

$$v_0 = -\frac{R^2}{4\rho\nu}\left(\frac{\Delta p}{L}\right), \tag{27}$$

with $\Delta p/L$ being the hydrostatic pressure difference along the length L of the pipe. Since $\Delta p < 0$, the velocity v_0 is always positive. As $t \to \infty$, the series expansion vanishes and the velocity approaches the asymptotic limit given by the first term on the right-hand side of Eq. (25). This solution corresponds to a paraboloid with the vertex (at $r = 0$) moving in the direction of the flow with velocity v_0.

For this test model, we first define a rectangular Cartesian box of sides $x = y = 1.27 \times 10^{-3}$ m and $z = 4.19 \times 10^{-4}$ m filled with a total number of 28,899 regularly arranged particles. The interparticle distance along the x and y axes is $\approx 3.33 \times 10^{-5}$ m, while that along the z-axis is $\approx 2.33 \times 10^{-5}$ m. A cylindrical pipe of radius $R = 5.0 \times 10^{-4}$ m and length $L = 2.33 \times 10^{-4}$ m is designed at the center of the box such that its circular cross-section coincides with the (x, y)-plane and its length is along the z-axis. With this choice, the magnitudes of ρ_0, v_0, and ν are the same as those of 2D Poiseuille flow at $Re = 0.0125$. For this configuration, the flow within the pipe volume is represented by 7799 particles, while the remaining 21,100 particles are used to fill the box region outside the pipe. The distribution of this outer particles is such that the space between both ends of the cylinder (at $z < 0$ and $z > L$) and the box surfaces in front of them is filled by rows of four particles each all along the z-direction. In the same way, along the x and y axes from the center of the cylinder, the space between the pipe surface and the other four box surfaces is also filled by rows of 4 particles each. The boundary conditions at the pipe surface are implemented by treating these outer particles as imaginary ones and using the same method of Morris et al. [9]. In this method, a normal distance d to the surface boundary is calculated for each fluid particle a close to the pipe surface. This normal is then used to define a plane tangent to the surface from which a second normal distance d' is calculated to the closest outer imaginary particle i. The velocity of particle a is extrapolated across the tangent plane (assuming that $\mathbf{v} = 0$ on the plane itself) such that $\mathbf{v}_i = -d'\mathbf{v}_a/d$. However, these velocities are not used to evolve the positions of the outer imaginary particles but just to compute viscous forces for those fluid particles that are close to the boundary surface. Inlet and outlet boundary conditions are applied at both extremes of the pipe by enforcing a cyclic boundary condition there. This is done in exactly the same way as for the 2D test cases by just treating the outer particles to the left ($z < 0$) and to the right ($z > L$) of the pipe as imaginary particles. In practice, accurate kernel estimates of the density for particles close to the boundary surface are obtained using no more than four imaginary particles along the normal to the surface. In this way, out of the 21,100 outer particles available only 13,652 are effectively used as true imaginary particles. This gives a total number of 21,451 effective particles. Inside the pipe region, the particles are initially at rest and were given a constant value of h ($= 3.5 \times 10^{-5}$ m) such that each particle has 50 neighbors within a sphere of radius $2h$.

The numerical results are shown in Fig. 3, where the computed velocity profiles (filled dots) are compared to the analytical solution (solid curves) given by Eq. (25) for a sequence of times until the steady-state profile is reached. The solution is shown over the full diameter D of the pipe. The dots on each curve represent mean

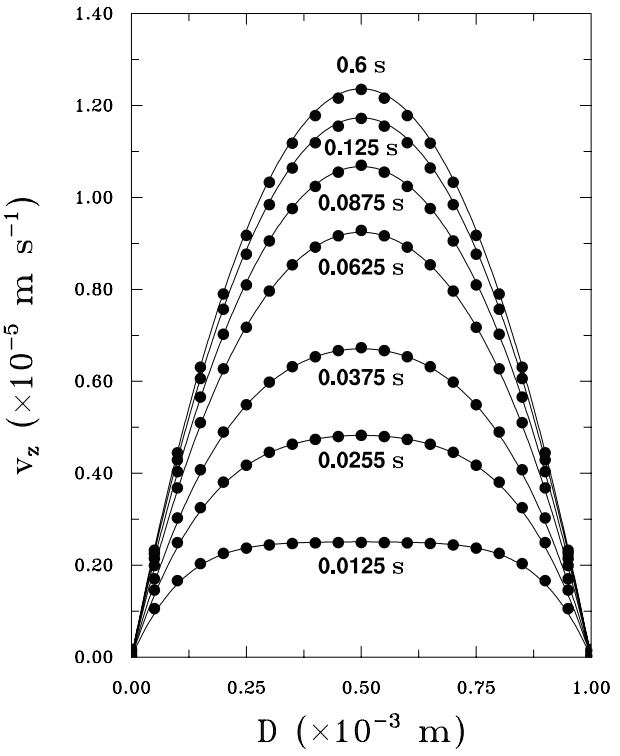

Fig. 3. Numerically obtained velocity profiles (filled dots) compared to the analytical solution (solid curves) for 3D Hagen–Poiseuille flow with $Re = 0.0125$ in a circular pipe of diameter $D = 2R = 1.0 \times 10^{-3}$ m. A sequence of times is shown for the transient evolution. The steady-state solution is reached at about 0.6 s.

values of the velocity for a given section of the pipe. In order to do this, we first take a section of pipe of size $\Delta z = L/20$ at approximately half its length. This results in a thin disk whose volume is further subdivided into a central disk of radius $\approx 3.34 \times 10^{-5}$ m around $r = 0$ plus 10 concentric annuli each of width $\approx 4.67 \times 10^{-5}$ m. In this way, the dots correspond to average velocities taken over all particles within each annulus. In the central disk, the average is taken over five particles, while in the outermost annulus the average is over 680 particles. By 0.6 s, the velocity profile reaches the steady-state solution with a numerically calculated value of $v_0 = 1.248 \times 10^{-5}$ m s^{-1}, corresponding to a relative error of about 0.2%. The incompressibility of the flow is very well reproduced with density variations within the range $0.993 \leqslant \rho/\rho_0 \leqslant 1.008$ throughout the pipe volume at all times. As for the 2D Poiseuille flow, the results shown in Fig. 3 were obtained using a cubic spline interpolation. When the same calculation is repeated using a quintic spline kernel, similar results to those displayed in Fig. 3 are obtained. Independently of the order of the kernel interpolation employed, the relative errors for this 3D test can be significantly lowered if a larger number of particles is used.

4. Formation of a liquid drop

So far we have tested the scheme for flow problems involving only the shear viscosity and where the fluid variables depend only on one spatial coordinate. The results of a more complicated test are presented here for the case of a van der Waals fluid in two dimensions, where both the coefficients of shear and bulk

viscosity are specified as separate parameters. In particular, we study the formation of a stable liquid drop at a temperature chosen such that no evaporation of the liquid will take place during the calculation. SPH simulations of the formation and dynamics of a circular drop floating in its vapor has been performed by Nugent and Posch [11]. Their SPH expressions for the motion and energy equations are the same as those displayed by Eqs. (8) and (18) and the density is computed from Eq. (1) so that their scheme is variationally consistent according to the analysis of Bonet and Lok [16]. In order to remove the tensile instability, which may affect this test case, the components of the viscous stress tensor have been modified by adding an artificial stress according to the prescriptions given by Gray et al. [19]. For a van der Waals fluid, these equations are closed by the constitutive relations

$$p = \frac{\rho \bar{k}_{\mathrm{B}} \mathcal{T}}{1 - \rho \bar{b}} - \bar{a}\rho^2 \tag{28}$$

and

$$U = \bar{k}_{\mathrm{B}} \mathcal{T} - \bar{a}\rho \tag{29}$$

for the pressure and specific internal energy, respectively. Here $\mathcal{T}$ is the fluid temperature, $\bar{k}_{\mathrm{B}} = k_{\mathrm{B}}/m$, $\bar{a} = a/m^2$, and $\bar{b} = b/m$, where k_{B} is the Boltzmann's constant, m is the particle mass, $a = \bar{\gamma}$ is the cohesive action accounting for the short-range attractive forces between neighboring molecules, and b is a constant parameter due to the finite size of the molecules. In two dimensions $b = 2\pi r_0^2$, where r_0 is the radius of a circular disk. For a van der Waals fluid model, the initial values of the density and temperature must satisfy the explicit conditions $\bar{k}_{\mathrm{B}}\mathcal{T} > 2\bar{a}\rho(1 - \rho\bar{b})^2$ and $\rho < 1/\bar{b}$ for thermodynamic stability. The first inequality results from guaranteeing that the specific heats as well as the product of the thermal expansion coefficient $\alpha = -(1/\rho)(\partial\rho/\partial T)_p$ and the Grüneisen coefficient $\Gamma = (1/\rho)(\partial p/\partial U)_\rho$ are always positive quantities. The same inequality also guarantees the positiveness of the isentropic bulk modulus $K_s = \rho(\partial p/\partial\rho)_s$, implying that the sound speed c belongs to a set of real numbers. The second inequality is a constraint on the density alone and comes out from the further requirement that the kinetic pressure, given by the first term on the right-hand side of Eq. (28), must also be positive. Combining this two inequalities with the positiveness of the basic thermodynamic states (ρ, $\mathcal{T}$, Γ) defines the domain of the phase space for this van der Waals model.

For this test, we use the same parameters as in Nugent and Posch [11]. That is, we take $m = 1$, $\bar{a} = 2$, $\bar{b} = 0.5$, and $\bar{k}_{\mathrm{B}} = 1$. In these reduced units, the critical point of the van der Waals fluid occurs for $\rho_{\mathrm{cr}} = 2/3$, $p_{\mathrm{cr}} = 8/27$, and $\mathcal{T}_{\mathrm{cr}} = 32/27$. Furthermore, for the coefficients of shear and bulk viscosity we choose $\eta = 1$ and $\zeta = 0.1$, respectively, while for the coefficient of thermal conductivity we take $\kappa = 5$. We choose the (x,y)-plane to represent the fluid. The initial configuration consists of $N = 900$ SPH particles of equal mass ($m_a = m$) uniformly distributed on a square Cartesian mesh of width $L_{\mathrm{m}} \approx 21.6$, as shown in Fig. 4(a). With these parameters the interparticle distance along the x- and y-direction is ≈ 0.72. In particular, we consider the same model calculation of Nugent and Posch [11] corresponding to their Fig. 1(a) for which an initial uniform temperature $\mathcal{T} = 0.2$ is assigned to each particle. At this subcritical value, a totally condensed circular drop with no external atmosphere is expected to form. Therefore, no periodic boundary conditions away from the initial array of particles is required for this test calculation. Since the mass is specified for each particle, the initial density profile is purposely calculated from the kernel estimate of the density, given by Eq. (1), in order to facilitate comparison with the results of Nugent and Posch [11]. Compared to their simulation, here we use a smaller number of particles and a correspondingly smaller smoothing length $h = 3$. Because of the crippling deficiency of particles at the boundaries of the initial configuration, the density there will be lower compared to the uniform initial value of interior particles. This produces an initial density distribution which is not discontinuous at the boundaries, thereby allowing the calculation to proceed without specifying any particular boundary condition. While this may affect the way in which the

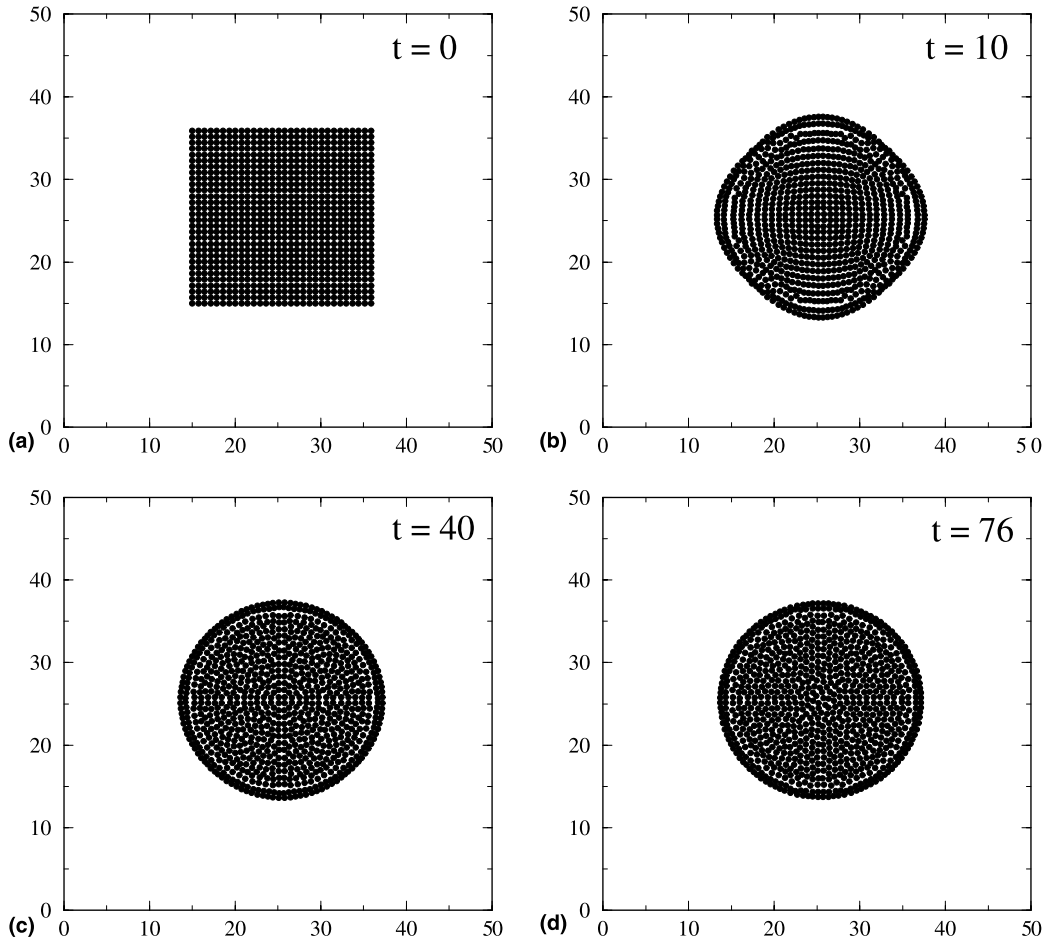

Fig. 4. Particle positions in the (x,y)-plane showing the formation of a stable van der Waals liquid drop. The initial temperature is $\mathcal{T} = 0.2$, while the critical temperature is $\mathcal{T}_{cr} \approx 1.19$ in our reduced units. A sequence of times is presented: (a) $t = 0.0$ (initial state); (b) $t = 10.0$; (c) $t = 40.0$; and (d) $t = 76.0$. In (d) equilibrium is fully reached.

surface tension depends on the temperature, a formal calculation for this test case will demand treating the outer boundary as a free surface.

The details of the drop condensation are clarified in Fig. 4, which shows the evolution for a sequence of times, starting from the initial state (Fig. 4(a)) and ending with the formation of a stable circular drop (Fig. 4(d)). The time is obtained by multiplying the number of computational cycles by the constant timestep size $\Delta t = 0.005$. About 15,200 cycles were required to complete the evolution. Compared to Fig. 1(a) of Nugent and Posch [11], we see that the inner structure of the forming drop in Fig. 4(d) is much more homogeneous. In their Fig. 1(a), the appearance of a well-defined pattern consisting of alternating dense rings and voids in the drop structure is the result of a tensile instability, which then disappears when appropriate corrections are applied to the viscous stress tensor on the right-hand side of Eqs. (8) and (18) [19]. For a detailed discussion of the corrections implemented and a complete set of drop model calculations showing a liquid-to-gas phase transition for higher subcritical temperatures, the reader is referred to Meleán et al. [20]. The rapid circularization of the drop (Fig. 4(b)) is one effect of the rising surface tension due to the pressure differences at the surface layer. The way in which the treatment of the outer boundary

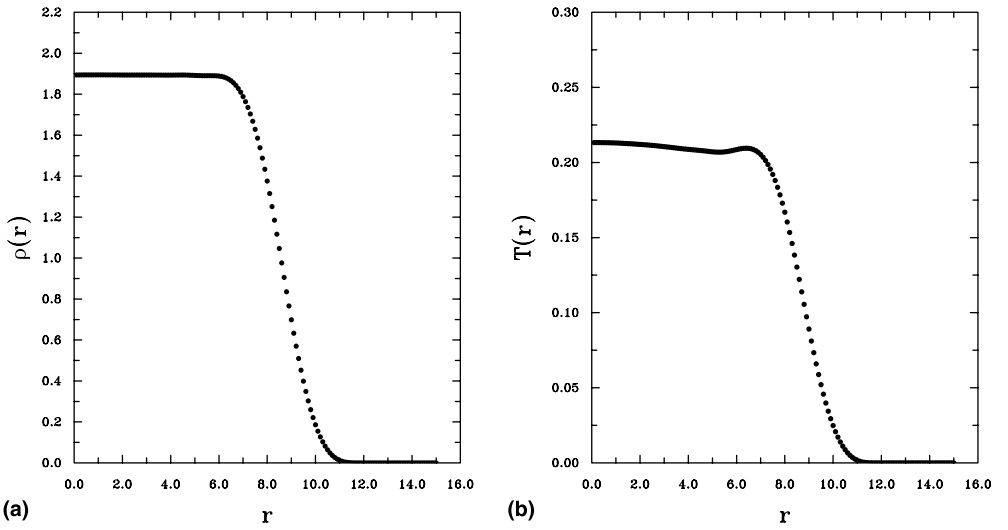

Fig. 5. (a) Average density and (b) temperature profiles across the drop configuration shown in Fig. 4(d) as a function of radius r. Here r means distance from the center of mass. All quantities are given in reduced units.

affects both the size and dependence of the surface tension with temperature is also being studied [21]. The radial density and temperature profiles for the equilibrium configuration of Fig. 4(d) are displayed in Figs. 5(a) and (b), respectively. We see that for most of the drop configuration, the density and temperature are almost constant followed by a monotonic rapid decay towards the outer layers. At equilibrium the density effectively obeys the inequality $\rho < 1/\bar{b} = 2$ as required by the positiveness of the kinetic pressure. Similarly, the temperature is such that the inequality $\bar{k}_B\mathcal{T} > 2\bar{a}\rho(1-\rho\bar{b})^2$ for thermodynamic stability is also satisfied.

5. Concluding remarks

A *working* Smoothed Particle Hydrodynamics (SPH) formalism for solving the equations of motion of a viscous fluid has been presented and tested. The scheme is based on standard SPH expressions for the first derivatives of the velocity to represent the viscous forces and is capable to produce accurate results for both compressible flows at high and moderate Reynolds numbers and incompressible flows at low Reynolds numbers.

Previous attempts to model these equations with SPH have relied on the use of a Gaussian kernel [7] which, being infinitely differentiable, guarantees evaluation of second-order derivatives in a stable manner. While this method was essentially applied to solving the Navier–Stokes equations for a constant shear viscosity, Flebbe et al. [14] and Watkins et al. [15] proposed independent new schemes for treating a general viscosity based only on standard SPH expressions for first derivatives. Unlike the method of Takeda et al. [7], the latter schemes allow the use of low-order kernels of compact support without the occurrence of significant instability. A variationally consistent SPH formulation for treating a general viscosity has been presented here, which is formally based on a standard symmetrized SPH representation of the equations of motion. In contrast with the method of Watkins et al. [15], the viscous forces are calculated by direct evaluation of the viscous stress tensor which involves only first-order derivatives of the velocity. In principle, the method is suitable for solving the equations of motion for a compressible viscous fluid for

arbitrary shear and bulk viscosities. When the scheme is combined with the pressure-gradient corrections proposed by Morris et al. [9], it also becomes suitable for solving the Navier–Stokes equations for incompressible flows at low Reynolds numbers without any further modification or assumptions.

In particular, we have presented tests for unsteady plane Poiseuille and Hagen–Poiseuille flows at $Re = 0.0125$ and $Re = 5$ using either a cubic or a quintic spline kernel. The results obtained for these test cases show a very good correspondence with the calculated analytical solutions and are essentially independent on the form of the kernel employed to perform the interpolation. Additional test simulations involving laminar flow through strongly curved ducts are presently been calculated. The method is also shown to perform well for the condensation of a 2D van der Waals liquid drop for which the effects of heat conduction are considered and the coefficients of shear and bulk viscosity enter as separate independent parameters. A modification of the scheme to handle boundary conditions of several types in a unified manner is currently being undertaken. This modified method is based on specialized SPH representations of the hydrodynamic equations for particles close to the boundary, and so it may treat different types of boundaries in almost the same manner and without the need of processing ghost or imaginary particles outside the computational volume.

Acknowledgements

The calculations of this paper were done using the computational facilities of the Laboratories of Computational Physics and Statistical Physics of Disordered Systems of the IVIC's Physics Center. This work is partially granted by an IVIC-2000 project on applied physics. One of us (J.K.) wishes to thank the Consejo Nacional de Ciencia y Tecnología (CONACyT) of Mexico and the Deutsche Forschungsgemeinschaft of Germany for partial support.

References

[1] H.L. Dryden, F.D. Murnaghan, H. Bateman, Hydrodynamics, Dover, New York, 1956.
[2] L.D. Landau, E.M. Lifshitz, Fluid Mechanics, Pergamon Press, Oxford, 1987.
[3] L.B. Lucy, A numerical approach to the testing of the fission hypothesis, Astron. J. 83 (1977) 1013.
[4] R.A. Gingold, J.J. Monaghan, Smoothed particle hydrodynamics: Theory and application to non-spherical stars, Mon. Not. R. Astron. Soc. 181 (1977) 375.
[5] W.G. Hoover, T.G. Pierce, C.G. Hoover, J.O. Shugart, C.M. Stein, A.L. Edwards, Molecular dynamics, smoothed-particle applied mechanics, and irreversibility, Comput. Math. Appl. 28 (1994) 155.
[6] J.J. Monaghan, Simulating free surface flows with SPH, J. Comput. Phys. 110 (1994) 399.
[7] H. Takeda, S.M. Miyama, M. Sekiya, Numerical simulation of viscous flow with smoothed particle hydrodynamics, Prog. Theor. Phys. 92 (5) (1994) 939.
[8] O. Kum, W.G. Hoover, H.A. Posch, Viscous conducting flows with smooth-particle applied mechanics, Phys. Rev. E 52 (5) (1995) 4899.
[9] J.P. Morris, P.J. Fox, Y. Zhu, Modeling low Reynolds number incompressible flows using SPH, J. Comput. Phys. 136 (1997) 214.
[10] S.J. Cummins, M. Rudman, An SPH projection method, J. Comput. Phys. 152 (1999) 584.
[11] S. Nugent, H.A. Posch, Liquid drops and surface tension with smoothed particle applied mechanics, Phys. Rev. E 62 (4) (2000) 4968.
[12] J.P. Morris, Stability properties of SPH, Publ. Astron. Soc. Aust. 13 (1996) 97.
[13] J.J. Monaghan, J.C. Lattanzio, A refined particle method for astrophysical problems, Astron. Astrophys. 149 (1985) 135.
[14] O. Flebbe, S. Münzel, H. Herold, H. Riffert, H. Ruder, Smoothed particle hydrodynamics: Physical viscosity and the simulation of accretion disks, Astrophys. J. 431 (1994) 754.
[15] S.J. Watkins, A.S. Bhattal, N. Francis, J.A. Turner, A.P. Whitworth, Astron. Astrophys. Suppl. Ser. 119 (1996) 177.
[16] J. Bonet, T.-S.L. Lok, Variational and momentum preservation aspects of Smoothed Particle Hydrodynamic formulations, Comput. Methods Appl. Mech. Engrg. 180 (1999) 97.

[17] L.D. Libersky, A.G. Petschek, T.C. Carney, J.R. Hipp, F.A. Allahdadi, High strain Lagrangian hydrodynamics, J. Comput. Phys. 109 (1993) 67.
[18] A.G. Petschek, L.D. Libersky, Cylindrical smoothed particle hydrodynamics, J. Comput. Phys. 109 (1993) 76.
[19] J.P. Gray, J.J. Monaghan, R.P. Swift, SPH elastic dynamics, Comput. Methods Appl. Mech. Engrg. 190 (2001) 6641.
[20] Y. Meleán, A. Hasmy, D. Broseta, E. Sira, L. Di G. Sigalotti, Liquid-to-vapor phase transition using SPH, Phys. Rev. E (in preparation).
[21] E. Sira, Y. Meleán, L. Di G. Sigalotti, A. Hasmy, A unified method for the treatment of boundary conditions in SPH, J. Comput. Phys. (in preparation).